Check for updates

Machine learning-assisted optimization of Cu-based HTLs for lead-free Sr₃PBr₃ perovskite solar cells achieving over 30% efficiency *via* SCAPS-1D simulation

Mahabur Rahman,[a] Md. Faruk Hossain,[b] Mongi Amami,[c] Lamia Ben Farhat,[c] Mutasem Z. Bani-Fwaz[c] and Md. Ferdous Rahman [ID] *[a]

The pursuit of efficient and stable lead-free perovskite solar cells (PSCs) is critical for sustainable photovoltaic technologies. In this work, we systematically investigated Sr₃PBr₃-based PSCs incorporating five different copper-based hole transport layers (HTLs)—Cu₂O, CuI, CuSbS₂, CuSCN, and Cu₂BaSnS₄ (CBTS)—using SCAPS-1D simulations. The device configuration FTO/SnS₂/Sr₃PBr₃/HTL/Au was optimized to evaluate the impact of HTL selection, absorber thickness, doping concentration, defect density, series resistance, and temperature on photovoltaic performance. The results demonstrate that the HTL choice strongly governs charge extraction, interfacial recombination, and stability. Among the candidates, CBTS exhibited the highest efficiency, achieving a power conversion efficiency (PCE) of 30.78% with an open-circuit voltage (V_{OC}) of 1.32 V, a short-circuit current density (J_{SC}) of 26.82 mA cm^{-2}, and a fill factor (FF) of 87.05%. Machine learning (ML) models trained on simulation datasets provided predictive accuracies above 99.6% and, through SHAP (SHapley Additive exPlanations) analysis, revealed that acceptor density and defect density are the most influential parameters controlling device performance. This combined simulation–ML framework establishes CBTS as a highly promising non-toxic HTL and provides actionable insights for the design of stable, high-efficiency lead-free PSCs.

1. Introduction

Driven by rapid technological advancements and population growth, the global energy demand continues to rise, yet its reliance on fossil fuels to meet these needs poses significant environmental challenges.[1] To tackle this issue, sustainable energy alternatives, such as solar energy conversion through photovoltaic (PV) technology, are being explored.[2–4] In recent decades, there have been major advancements in the development of solar cells, including those made from GaAs, Si, CdTe, and CIGS.[5–8] Recent reports reveal that GaAs has achieved a record power conversion efficiency (PCE) of up to 27.6%. However, the epitaxial growth process needed for GaAs layers significantly increases the cost of these solar cells.[5] In contrast, approximately 90% of the photovoltaic market depends on

Si-based cells.[6] However, Si solar cells have several disadvantages, including being an indirect semiconductor[9] and having a low absorption coefficient. This necessitates the use of a thick absorber layer, which increases costs due to the requirement for a substantial amount of high-quality single-crystal silicon.[10,11] It is noteworthy that materials with direct bandgaps, such as CdTe and CIGS, are commonly employed in commercial solar cell technologies.[12] However, these materials encounter difficulties because of the limited availability of elements on the Earth. Despite the reports on Cu₂ZnSn(S,Se)₄ (CZTSSe), which exists more extensively in the Earth's surface layer, the achieved PCE remains significantly lower at 14.9% compared to other established materials.[13] Conversely, the rise of organic–inorganic lead halide perovskites (MAPbX₃, where X = I, Br, and Cl) has sparked significant attention to the advancement of photovoltaic materials.[14] Perovskite materials have demonstrated remarkable advancement, with their PCE enhancing dramatically from 3.8% in 2009 to a remarkable value of 26.1% by 2023. This places them as extremely promising contenders in the photovoltaic domain. Despite their outstanding performance, there are concerns regarding the poisonousness of lead and the stability of halides, which

[a] Advanced Energy Materials and Solar Cell Research Laboratory, Department of Electrical and Electronic Engineering, Begum Rokeya University, Rangpur, 5400, Bangladesh. E-mail: ferdousapee@gmail.com

[b] Department of Physics, Rajshahi University of Engineering & Technology, Rajshahi, 6204, Bangladesh

[c] Department of Chemistry, College of Science, King Khalid University, P.O. Box 9004, Abha, 61413, Saudi Arabia

present hurdles to their durability over time and viability in the market.[15–17]

In response to these concerns, scientists are enthusiastically investigating lead-free substitutes with the goal of addressing environmental issues and laying the groundwork for the next era of perovskite-based technologies.[18] More precisely, perovskites based on tin (Sn) and germanium (Ge), for example, $MASnI_3$, $CsSnI_3$, $FASnI_3$, $CsGeI_3$, $MAGeI_3$, and $FAGeI_3$, have emerged as promising substitutes due to their lack of toxicity, narrow bandgaps, and superior carrier mobility.[19] Despite their promise, issues related to stability remain. For example, Sn^{2+} and Ge^{2+} ions are susceptible to oxidation, leading to their conversion into Sn^{4+} and Ge^{4+} when exposed to the surrounding atmosphere. Furthermore, the scarcity of Ge in the Earth's crust and its high cost further limit its practical application.[20,21] Indeed, scientists have recognized various alternative strategies. One approach entails the application of trivalent cations like Bi^{3+} and Sb^{3+} in lieu of Pb^{2+} ions. However, the achieved power conversion efficiency (PCE) with these replacements notably lags behind that of lead halide perovskites. This disparity could stem from their intrinsically low-dimensional structure, resulting in their unfavorable optoelectronic properties.[22]

Recently, researchers have increasingly employed SCAPS-1D simulations to gain deeper insights into the physical behavior of PSCs.[23] This approach has helped them fine-tune various components of the devices, leading to more efficient designs.[24] Moreover, machine learning has proven to be an effective approach for identifying novel methods to optimize the design and efficiency of PSCs.[25] Studies have shown that machine learning is an effective tool for predicting both the material characteristics and efficiency outcomes of PSCs.

To address these obstacles, researchers have introduced halide double perovskites (HDPs), featuring a structure resembling $A_2B^+B^{3+}X_6$, where A and B^+/B^{3+} represent cations and X indicates anions.[26] This advancement entails replacing Pb^{2+} with environmentally friendly Bi^{3+} while keeping a three-dimensional configuration.[27] This advanced approach involves substituting two Pb^{2+} ions with one B^+ ion and one B^{3+} ion. Noteworthy samples of such HDPs include $(CH_3NH_3)_2KBiCl_6$, $(CH_3NH_3)_2AgBiBr_6$, $Cs_2AgBiBr_6$, and $Cs_2NaBiCl_6$, which have recently attracted significant attention as highly favorable materials.[28] Despite their potential, HDPs encounter limitations such as weak charge carrier transport capabilities, high effective masses of charge carriers, and a high bandgap exceeding 2 eV.[29] Hence, research endeavors have concentrated on investigating antimony-based perovskite materials, including $Cs_2SbAgCl_6$, Cs_2SbAgI_6, $Cs_2SbCuCl_6$, $Cs_4SbCuCl_{12}$, and $Cs_2SbAgBr_6$. These materials are acknowledged for their capacity to endure high temperatures and promote effective carrier mobility. Nonetheless, their prospects are constrained by wide bandgaps, elevated binding energies, and augmented carrier effective mass.[30,31] Consequently, there is an urgent requirement to identify novel materials that can preserve the remarkable characteristics of lead halide perovskites while mitigating the mentioned drawbacks.

As Sr_3PBr_3 is an emerging perovskite material, its crystal structure formation is influenced by the chemical interactions between Sr^{2+} cations and PBr_3 units, which stabilize the lattice through ionic bonding and maintain charge neutrality. The perovskite framework arises from the corner-sharing octahedral arrangement of $SrBr_6$ units, with P^{3+} ions occupying the interstitial sites, promoting structural stability. Among the various perovskite compositions explored, Sr_3PBr_3 has recently appeared as a promising absorber material due to its favorable optoelectronic properties and environmental safety.[32,33] This ternary halide features a stable orthorhombic crystal structure derived from alkaline earth and halide elements, which offers intrinsic thermal and structural stability under ambient conditions.[32,33] With a direct bandgap of 1.528 eV, Sr_3PBr_3 falls within the optimal range for single-junction solar cells according to the Shockley–Queisser limit, making it highly suitable for efficient solar energy conversion.[32,33] Furthermore, it exhibits a strong absorption coefficient across the visible spectrum and a low toxicity profile, in contrast to conventional Pb-based perovskites. Unlike Sn- and Ge-based alternatives, Sr_3PBr_3 is less susceptible to oxidation-induced instability, as it lacks divalent metal cations prone to environmental degradation (e.g., $Sn^{2+} \rightarrow Sn^{4+}$). Preliminary theoretical and experimental studies have shown that Sr_3PBr_3 can achieve long carrier diffusion lengths and low recombination rates, indicating strong potential for photovoltaic applications.[34]

One critical component in PSCs that significantly influences their performance is the hole transport layer (HTL). The HTL efficiently extracts and transfers holes from the perovskite absorber to the anode, reducing recombination losses and boosting device efficiency. Copper-based HTLs, such as Cu_2O, CuI, $CuSbS_2$, CuSCN, and CBTS, have shown promise due to their favorable energy levels, high absorption coefficient, non-toxicity, good hole mobility, and chemical stability.[35,36]

The device structure under investigation in this study is FTO/SnS_2/Sr_3PBr_3/Cu-based HTLs/Au. Employing fluorine-doped tin oxide (FTO) as the front electrode alongside SnS_2 as the electron transport layer (ETL) ensures good conductivity and electron extraction. Sr_3PBr_3 serves as the active layer, with the copper-based HTLs facilitating hole transport to the gold (Au) back contact. The choice of multiple HTLs allows for a comparative analysis of their impact on device performance.

To optimize the device architecture and predict performance metrics, we employed the SCAPS-1D simulation software.[37,38] SCAPS-1D is a well-established tool for modeling and simulating the electrical characteristics of PSCs, revealing the role of multiple parameters in determining device efficiency. By systematically varying the absorber thickness, defect density, and acceptor concentration, along with adjustments to the ETL and HTL thicknesses and operating temperature, this study seeks to determine the optimal configuration that maximizes the PCE of Sr_3PBr_3-based PSCs.

In addition to these material considerations, the performance of any single-junction photovoltaic device is fundamentally constrained by the Shockley–Queisser (SQ) limit, which defines the maximum theoretical values of J_{SC}, V_{OC}, FF, and

PCE as a function of the absorber bandgap under AM1.5 illumination. According to the theoretical framework outlined by Morales-acevedo in 2023, an absorber with a bandgap of 1.528 eV, such as Sr_3PBr_3, possesses an upper-limit V_{OC} of approximately 1.30–1.40 V and a maximum efficiency near 30%.[39] Therefore, in this work, all simulated device parameters were revised and analyzed to ensure consistency with these physical constraints, preventing overestimation of photovoltaic performance. This alignment with the SQ-limit framework guarantees that the simulation results remain physically meaningful and theoretically justified.

2. Device configuration and simulation

2.1. Simulated device configurations

In our research, we evaluated the performance of novel Sr_3PBr_3-based PSCs with five different inorganic Cu-based HTLs, namely CBTS, Cu_2O, CuI, $CuSbS_2$, and CuSCN, using SCAPS-1D simulation. The configuration mimics a superstrate setup of $FTO/SnS_2/Sr_3PBr_3/HTL/Au$, as illustrated in Fig. 1. Initial parameters for individual layers were obtained from the existing literature and are detailed in Table 1. Throughout the simulations, the thermal velocities of holes and electrons were fixed at
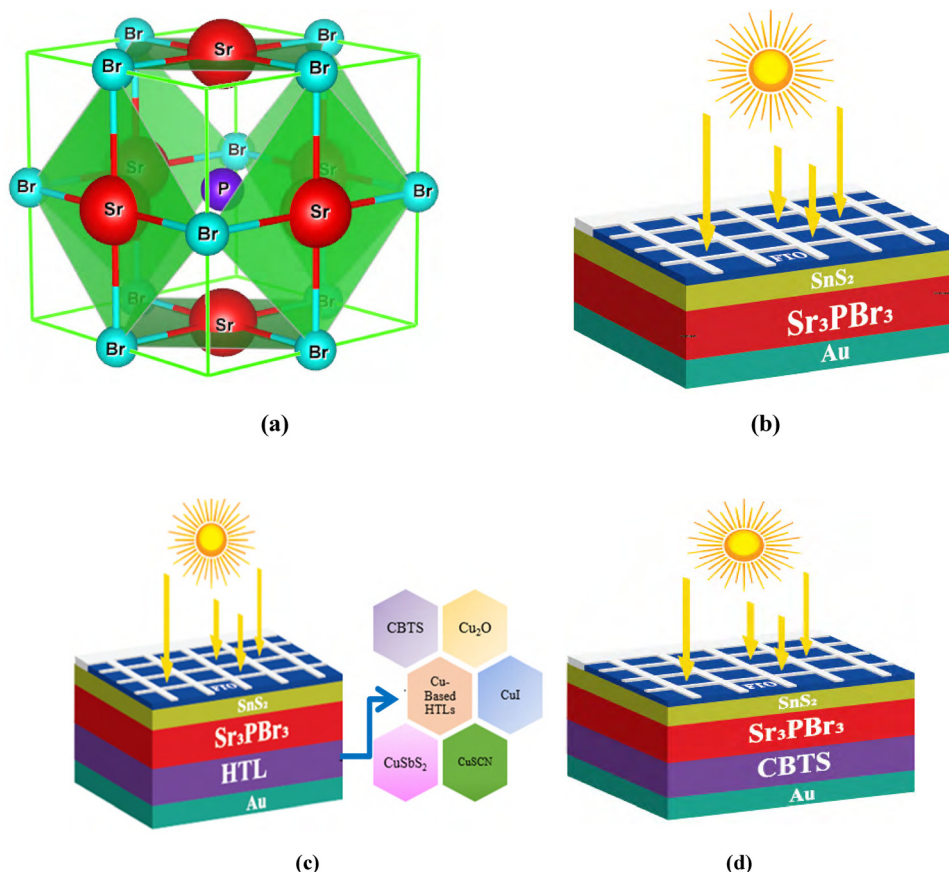

Fig. 1 (a) Crystal structure of the novel Sr_3PBr_3 and a schematic of Sr_3PBr_3-based solar cells, (b) without an HTL, (c) with various inorganic Cu-based HTLs, and (d) with the optimized HTL.

Table 1 Input parameters employed in the simulation of the proposed PSCs[40–47]

Parameters	Terms	FTO	SnS_2	Sr_3PBr_3 (ref. 32 and 33)	Cu_2O	CBTS	CuI	CuSCN	$CuSbS_2$
t (μm)	Thickness	0.05	0.05	1	0.05	0.05	0.05	0.05	0.05
E_g (eV)	Bandgap	3.6	2.42	1.528	2.17	1.90	3.10	3.40	1.580
χ (eV)	Electron affinity	4.5	4.24	4.160	3.2	3.60	2.1	1.9	4.2
ε_r	Relative permittivity	10	10	5.280	7.11	5.4	6.5	10	14.6
N_c (cm^{-3})	Eff. DOS at the CB	2×10^{18}	2×10^{18}	1.185×10^{19}	2.02×10^{17}	2.2×10^{18}	2.8×10^{19}	2.2×10^{18}	2×10^{18}
N_v (cm^{-3})	Eff. DOS at the VB	1.8×10^{19}	1.8×10^{18}	1.660×10^{19}	1.1×10^{19}	1.8×10^{19}	1×10^{19}	1.8×10^{18}	1×10^{19}
μ_n (cm^2 (V s)$^{-1}$)	Electron mobility	100	50	25	200	300	100	100	49
μ_p (cm^2 (V s)$^{-1}$)	Hole mobility	20	50	20	80	100	43.9	25	49
N_A (cm^{-3})	Dopant density (acceptor)	0	0	1×10^{17}	1×10^{18}	1×10^{18}	1×10^{18}	1×10^{18}	1×10^{18}
N_D (cm^{-3})	Dopant density (donor)	1×10^{18}	1×10^{17}	0	0	0	0	0	0
N_t (cm^{-3})	Defect density	1×10^{14}	1×10^{12}	1×10^{12}	1×10^{15}	1×10^{15}	1×10^{15}	1×10^{15}	1×10^{15}

Table 2 Input parameters at the ETL/Sr$_3$PBr$_3$ and Sr$_3$PBr$_3$/HTL interfaces

Interface	Defect type	Capture cross section: electrons/holes (cm^2)	Defect position above the highest EV (eV)	Energetic distribution	Reference for the defect energy level	Total density (cm^{-2}) (integrated overall energies)
HTL/Sr$_3$PBr$_3$	Neutral	1×10^{19}	0.06	Single	Above the VB maximum	1.0×10^{10}
Sr$_3$PBr$_3$/ETL	Neutral	1×10^{19}	0.06	Single	Above the VB maximum	1.0×10^{10}

10^7 cm s^{-1} for every layer, with a flat-band condition applied to the front contact. The simulations were performed at 300 K under AM 1.5G spectral irradiance. To more accurately replicate real operating conditions, neutral defects were incorporated at the ETL/Sr$_3$PBr$_3$ and Sr$_3$PBr$_3$/HTL interfaces, using the parameters specified in Table 2.

2.2. Mathematical modeling

SCAPS-1D is an advanced simulation tool specifically designed to analyze the performance of solar cells, and it is widely utilized for evaluating various types of photovoltaic devices.[48,49] It offers the photovoltaic research community comprehensive insights into key output parameters, enabling a deeper understanding of device behavior. This capability is realized by numerically solving three fundamental equations integrated into the SCAPS-1D framework: the Poisson eqn (1), the continuity eqn (2) and (3), and the charge transport eqn (4) and (5), which collectively govern charge carrier dynamics. These equations are expressed as follows[50,51]:

$$\frac{\partial^2 \varphi}{\partial x^2} = \frac{q}{\varepsilon}(n(x) - p(x) + N_A(x) - N_D(x) - p_t(x) - N_t(x)) \quad (1)$$

where q denotes the elementary charge, ε represents the dielectric constant, p indicates the hole concentration, and n corresponds to the electron concentration. Furthermore, N_D refers to the doping concentration of donor-type impurities, while N_A denotes the doping concentration of acceptor-type impurities.

$$\frac{\partial n}{\partial t} = \frac{1}{q}\frac{\partial J_n}{\partial x} + (G_n - R_n) \quad (2)$$

$$\frac{\partial p}{\partial t} = -\frac{1}{q}\frac{\partial J_p}{\partial x} + (G_p - R_p) \quad (3)$$

Here, G_n denotes the electron generation rate, while G_p represents the hole generation rate. Similarly, R_n corresponds to the electron recombination rate, and R_p signifies the hole recombination rate. The symbols J_p and J_n indicate the current densities of holes and electrons, respectively.[52]

$$J_n = qD_n\frac{\partial n}{\partial x} - q\mu_n n\frac{\partial \varphi}{\partial x} \quad (4)$$

$$J_p = qD_p\frac{\partial p}{\partial x} - q\mu_p p\frac{\partial \varphi}{\partial x} \quad (5)$$

where D_n represents the electron diffusion coefficient, while D_p corresponds to the hole diffusion coefficient. Similarly, μ_n denotes the electron mobility, and μ_p signifies the hole mobility.

3. Results and discussion

3.1. Initial solar cell performance

The original solar cells are constructed using the configuration FTO/SnS$_2$/Sr$_3$PBr$_3$/HTL/Au, as depicted in Fig. 1, where inorganic HTLs like CBTS, Cu$_2$O, CuI, CuSbS$_2$, and CuSCN have been used. The photovoltaic parameters of the new Sr$_3$PBr$_3$-based PSCs are presented in Table 3. Specifically, the power conversion efficiencies (PCEs) are 30.78%, 28.59%, 23.27%, 26.09%, and 27.92% for HTLs based on CBTS, Cu$_2$O, CuI, and CuSbS$_2$, respectively, and 20.80% without an HTL.[48,49] Table 3 shows the maximum parameters achieved under optimal temperature conditions.

3.2. Bandgap configuration of a Sr$_3$PBr$_3$-based PV system

The alignment of the energy band influences the current flow in a heterostructure. In our research, we examined various HTLs to determine which one provides the best PCE. Specifically, we utilized HTLs such as Cu$_2$O (Fig. 2(c)), CuI (Fig. 2(d)), and CuSbS$_2$ (Fig. 2(e)). Fig. 2(a) displays the refined energy band diagram without an HTL, whereas Fig. 2(b) shows the band configuration incorporating the HTL (CBTS), which provides a superior PCE compared to the other HTLs. The results from the SCAPS simulation provide insights into the bandgap and thickness of each layer, highlighting the band bending at the interface of the CBTS and Sr$_3$PBr$_3$ layers, providing more favorable band alignment, especially with different doping levels.

This bending promotes accelerated electron mobility in Sr$_3$PBr$_3$-based photovoltaic cells, enhancing the photovoltaic cell's capability for peak efficiency. The band energy diagram provides precise predictions of how holes and electrons move within the designed PSC, despite a minor offset that does not impede carrier transport, as it remains below thermal energy levels.

The alignment of the energy bands plays a pivotal role in governing current flow within a heterostructure.[53–55] In this study, we systematically investigated several HTLs to identify

Table 3 Obtained photovoltaic parameters of Sr$_3$PBr$_3$ solar cells

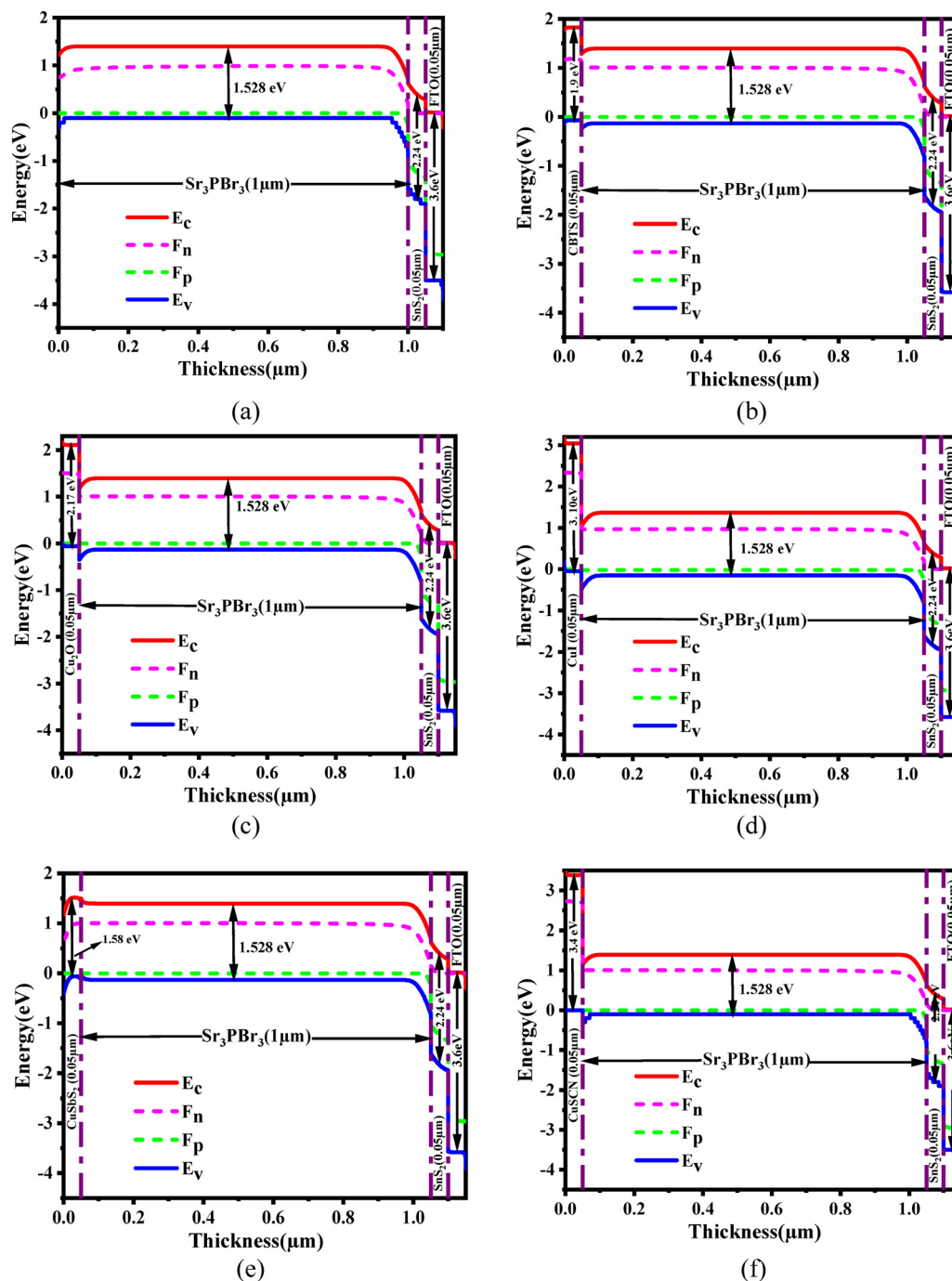| Structure of PSCs	V_{OC} (V)	FF (%)	J_{SC} (mA cm^{-2})	PCE (%)
Without an HTL				
FTO/SnS$_2$/Sr$_3$PBr$_3$/Au	1.052	86.13	22.971	20.80
With an HTL				
FTO/SnS$_2$/Sr$_3$PBr$_3$/CuI/Au	1.101	84.32	25.050	23.27
FTO/SnS$_2$/Sr$_3$PBr$_3$/CuSbS$_2$/Au	1.111	88.82	26.429	26.09
FTO/SnS$_2$/Sr$_3$PBr$_3$/CuSCN/Au	1.237	84.31	26.762	27.92
FTO/SnS$_2$/Sr$_3$PBr$_3$/Cu$_2$O/Au	1.255	84.96	26.808	28.59
FTO/SnS$_2$/Sr$_3$PBr$_3$/CBTS/Au	1.317	87.05	26.839	30.78

Fig. 2 Band configuration of a Sr_3PBr_3-based photovoltaic cell (a) without an HTL and with an HTL: (b) CBTS, (c) Cu_2O, (d) CuI, (e) $CuSbS_2$, and (f) CuSCN.

the one that delivers the highest PCE. Specifically, HTLs including Cu_2O (Fig. 2(c)), CuI (Fig. 2(d)), and $CuSbS_2$ (Fig. 2(e)) were evaluated. For comparison, Fig. 2(a) illustrates the optimized energy band diagram of the device without an HTL, while Fig. 2(b) presents the detailed insights into the bandgap configuration incorporating CBTS as the HTL, which demonstrated superior PCE relative to the other candidates, revealing pronounced band bending at the $CBTS/Sr_3PBr_3$ interface. This favorable band alignment, particularly under varying

doping concentrations, facilitates more efficient charge separation and transport. The observed band bending accelerates electron extraction and transport in Sr_3PBr_3-based PSCs, thereby enhancing the device's capability to achieve peak performance. Furthermore, the energy band diagram accurately predicts the movement of charge carriers within the architecture, where the minimal offset present does not hinder carrier transport, as it remains well below the thermal energy threshold. Therefore, CBTS was selected as the optimized HTL and

employed in all subsequent simulations and analyses throughout the remainder of this study.

3.3. Impact of Sr_3PBr_3 layer thickness and doping concentration

Fig. 3(a) illustrates the effect of varying the thickness of the absorber on the output characteristics of Sr_3PBr_3-based PSCs with and without the CBTS HTL. As the perovskite Sr_3PBr_3 layer becomes thicker in the configurations, the J_{SC} increases, achieving a peak value of 26.839 mA cm^{-2} at 1.0 μm. Subsequently, J_{SC} increases slightly with further thickness because recombination dynamics influence charge separation in the PV cell. Moreover, with a Sr_3PBr_3 thickness of 1.0 μm, the overall absorption is predicted to escalate, leading to a higher exciton production rate and consequently increasing electron creation in the absorber layer due to improved photon absorption. Additionally, the changes in V_{OC} with varying Sr_3PBr_3 thicknesses from 0.1 μm to 2.0 μm are presented. The V_{OC} attains its maximum at a thickness of 1.0 μm and then remains relatively constant, a trend primarily governed by recombination dynamics at higher thicknesses. With increasing thickness of the absorber layer, there is typically a corresponding rise in the

device's FF, potentially leveling off around a thickness of 1.0 μm. Changes in performance across different thicknesses of Sr_3PBr_3 in PV cells are evident, influenced directly by thickness variations affecting FF, V_{OC} and J_{SC}, with peak efficiency observed around 1.0 μm, which is therefore chosen as the optimized absorber thickness. A perovskite's advantage lies in its ability to absorb a broader spectrum of photons across a wider range of frequencies, attributed to its larger bandgap.[56] With 1.0 μm thickness, the diffusion distances are L_p = 34 μm and L_n = 34 μm.

Enhancing the output of the PV cell involves precisely doping the absorber material.[57] Nevertheless, extreme doping may present challenges owing to its non-traditional nature, possible hindrance to carrier transport and added structural complexity in manufacturing. Therefore, the active layer doping density was changed from 10^{12} cm^{-3} to 10^{20} cm^{-3} in simulations to ascertain the optimal value. Fig. 3(b) depicts how varying the N_A affects the Sr_3PBr_3 absorber layer without and with the CBTS HTL. The goal was to raise the V_{OC} from 1.316 V to 1.425 V with the HTL and 0.840 V to 1.241 V without the HTL, adjusting N_A of the Sr_3PBr_3 material from 10^{12} cm^{-3} to 10^{20} cm^{-3}. The J_{SC} rises from 26.799 to 26.841 mA cm^{-2} with

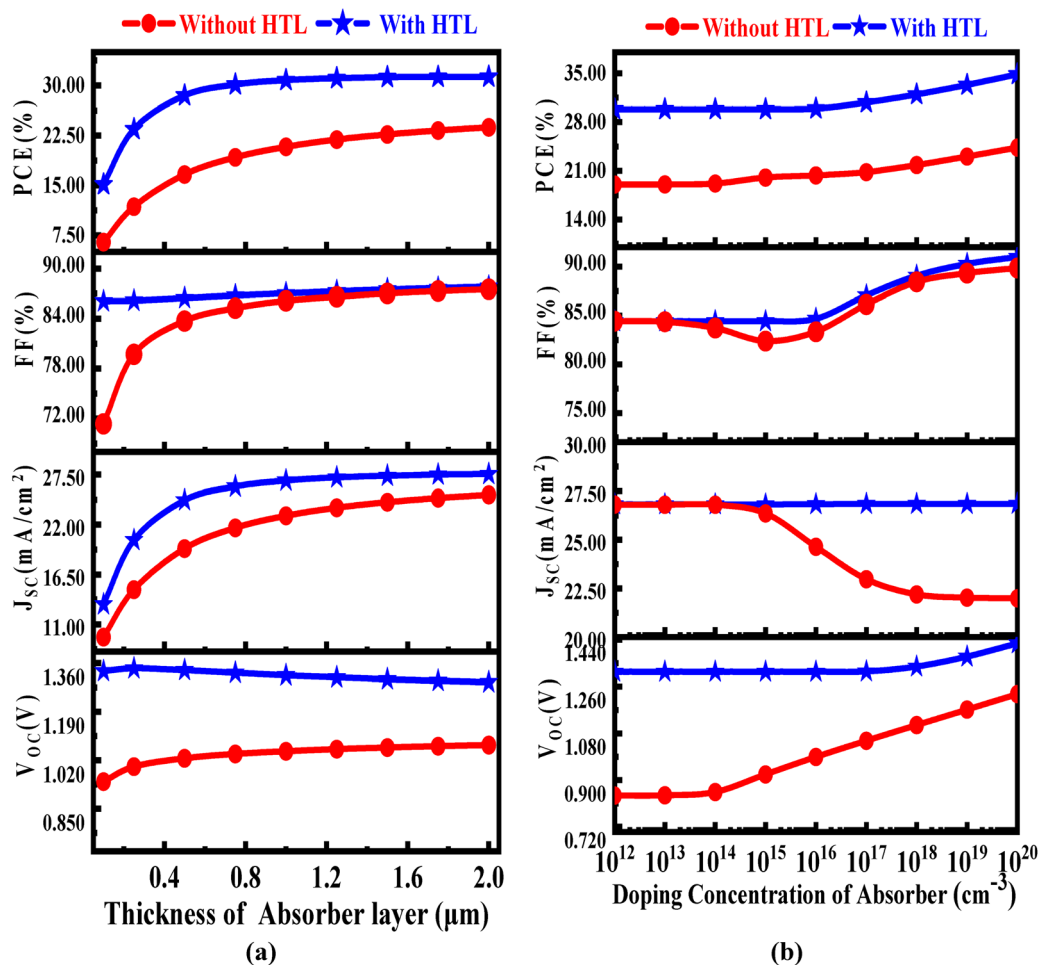**Fig. 3** Impact of varying (a) the thickness of Sr_3PBr_3 and (b) the doping density in Sr_3PBr_3, without and with the CBTS HTL.

the HTL and it reduces from 26.789 to 21.988 mA cm^{-2} without the HTL. The FF and PCE show a slight increase from 10^{12} cm^{-3} to 10^{20} cm^{-3} for both the cases.

3.4. Effect of changes in absorber thickness and density of defect on solar cell performance

The absorber layer's thickness and defect density play a crucial role in determining solar cell performance. An enhancement in defects causes the film to deteriorate and form pinholes, leading to higher recombination rates that degrade the steadiness and PCE of PSCs.[58] Therefore, to determine the optimal defect density for a given absorber layer thickness, simulations were carried out with absorber thicknesses ranging from 0.1 μm to 2.0 μm, while adjusting the defect value from 10^{10} cm^{-3} to 10^{16} cm^{-3}. Fig. 4(a–d) illustrates the variations in J_{SC}, V_{OC}, FF, and PCE for the FTO/SnS$_2$/Sr$_3$PBr$_3$/CBTS/Au device configuration, providing a comprehensive depiction of how each photovoltaic parameter responds to the applied simulation conditions. It is apparent that the solar cells achieved peak V_{OC} values for absorber layer thicknesses ranging from 0.3 μm to 2.0 μm and defect densities between 10^{10} cm^{-3} and 10^{12} cm^{-3}. This enhancement is due to the increase in quasi-Fermi level separation as the thickness increases.[59]

Fig. 4(a) depicts how the J_{SC} values vary with active layer thickness and defect density. Upon analyzing the contour plots, a consistent pattern emerges across all solar cells regarding these variables. Remarkably, the solar cell reached its peak J_{SC} value when the thickness of the active layer surpassed 1.0 μm, while maintaining a defect density below 10^{12} cm^{-3}. This rise in J_{SC} values is due to improved spectral response at greater thicknesses and minimized charge carrier recombination.[60] Fig. 4(c) illustrates the impact on FF, highlighting an optimal thickness of 1.0 μm while keeping the defect density below 10^{12} cm^{-3}. Fig. 4(d) depicts how changing the defect density and absorber thickness impacts the PCE. Increasing the absorber thickness enhances the PCE, while increasing the defect density decreases it.

3.5. Impact of ETL thickness and donor density

An ETL is essential for improving light transmittance and reducing recombination inside PSCs.[61] Hence, it is crucial to adjust the characteristics of charge transport layers accordingly. In this research, we adjusted the SnS$_2$ thickness from 0.03 to 0.3 μm while keeping all other parameters unchanged as shown in Fig. 5(a)–(d). Fig. 5(a) illustrates the effect of ETL thickness on the photovoltaic output. The variation in SnS$_2$
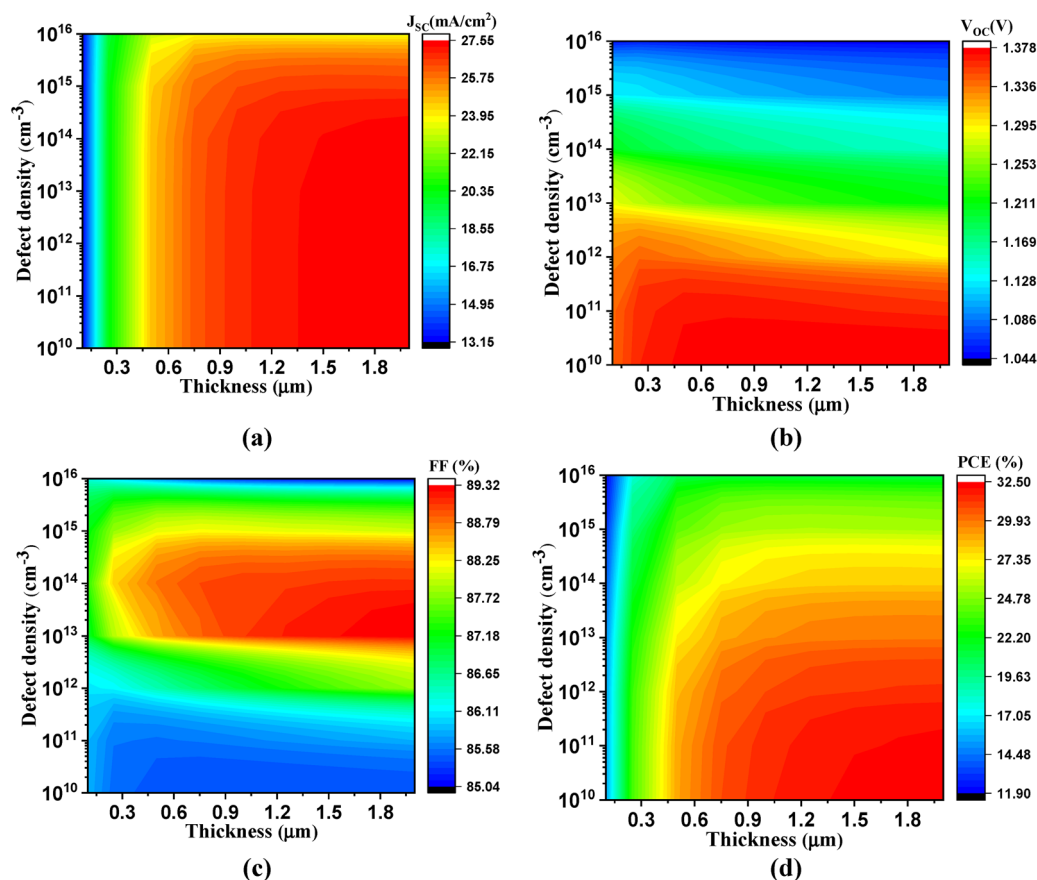

Fig. 4 Contour plots illustrating the impact of photovoltaic performance metrics due to variations in active layer thickness and defect density: (a) J_{SC}, (b) V_{OC}, (c) FF and (d) PCE.
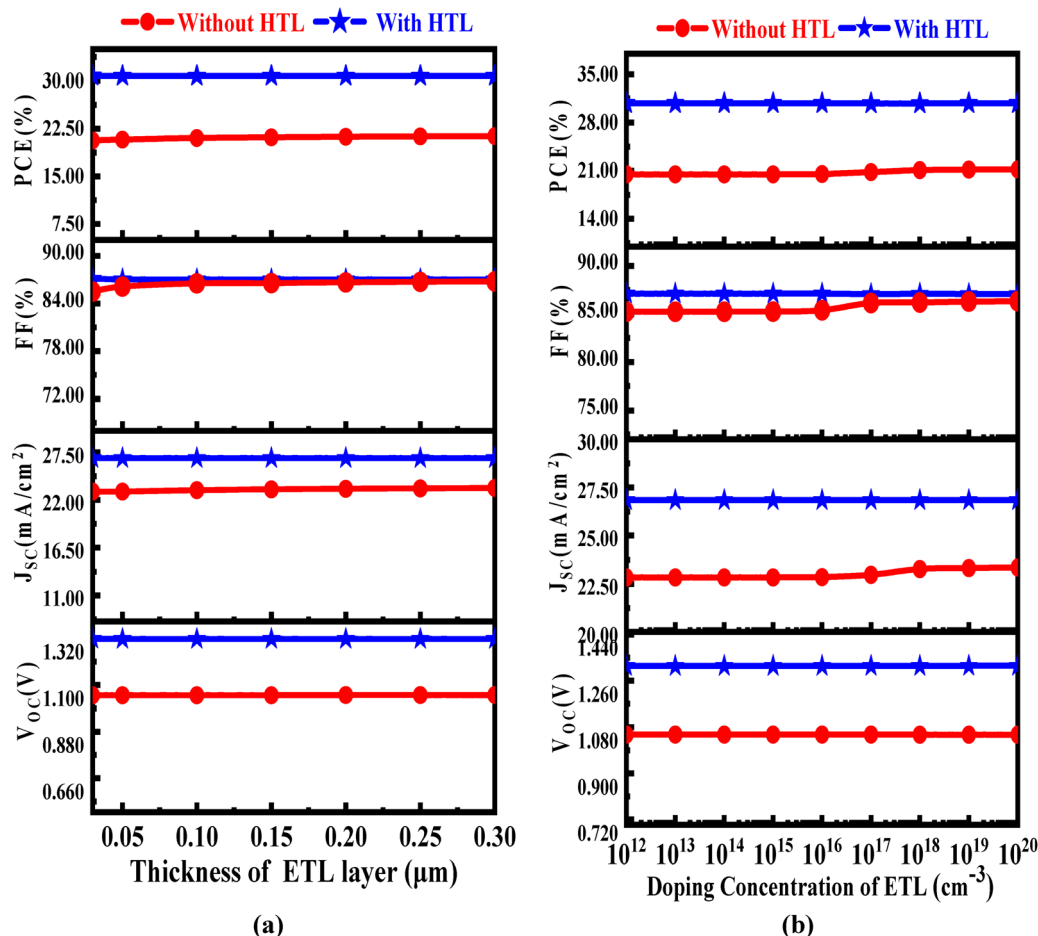
Fig. 5 Effect of varying the (a) thickness of SnS_2, without and with the CBTS HTL, and (b) donor concentration in SnS_2, without and with the CBTS HTL.

thickness has an almost negligible effect on J_{SC}, with values ranging only slightly from 26.840 mA cm^{-2} at 0.03 μm to 26.831 mA cm^{-2} at 0.3 μm. For V_{OC}, a comparable trend is observed. Significantly, the peak efficiency of 30.78% is accomplished with an SnS_2 layer thickness of 0.05 μm. Fig. 5(b) demonstrates the effect of varying the N_D within the ETL (SnS_2) on the performance of the proposed PSC device, spanning from 10^{12} to 10^{20} cm^{-3}. It has been observed that with an increase in the ETL doping concentration, V_{OC} remains the same for both conditions, whereas J_{SC} shows a marginal enhancement of up to 10^{16} cm^{-3}, after which it exhibits a significant upsurge. Up to 10^{16} cm^{-3}, FF and PCE almost maintain a constant trend with doping concentrations in the HTL.

3.6. Impact of defect density at the ETL/Sr$_3$PBr$_3$ and HTL/Sr$_3$PBr$_3$ interfaces

During the fabrication of solar cells, interface defects arise from structural defectiveness. These defects upsurge charge carrier recombination at the interface, thereby compromising the PSC's performance.[62] Therefore, investigating their impact and estimating optimal values for practical production is crucial. In our analysis, a neutral interface defect density of 10^{10} cm^{-2} was applied at both the ETL/Sr$_3$PBr$_3$ and Sr$_3$PBr$_3$/HTL

interfaces, with defect levels maintained at 0.6 eV across all PV cells. Here, we evaluate the impact of interface defect density (IDD) on the PV output by changing it from 10^{10} cm^{-2} to 10^{16} cm^{-2} with the thickness ranging from 0.1 to 2.0 μm for both interfaces. Fig. 6 shows that changing the IDD between CBTS and Sr$_3$PBr$_3$ affects the performance of the PSC. The J_{SC}, FF, PCE, and V_{OC} of the Sr$_3$PBr$_3$-based PSCs decline from 27.50 mA cm^{-2} to 11.10 mA cm^{-2}, 87.8% to 70.70%, 31.3% to 7.49%, and 1.341 V to 0.957 V, respectively, when the IDD is changed from 10^{10} cm^{-2} to 10^{16} cm^{-2} at the Sr$_3$PBr$_3$/CBTS interface.

Fig. 7 shows the results of SnS_2/Sr$_3$PBr$_3$ interface defects. At the SnS_2/Sr$_3$PBr$_3$ interface, a higher interface defect density significantly impacts the J_{SC}, which decreases from 27.52 to 13.25 mA cm^{-2}. Additionally, the V_{OC} drops from 1.33 V to 0.795 V, the FF reduces from 87.85% to 75.52%, and the PCE declines from 31.30% to 7.93%.

3.7. Influence of series and shunt resistance

Parasitic resistances, such as R_S and R_{SH}, are crucial factors in solar cell output. They affect the current–voltage (J–V) characteristics of the PSCs and represent sources of energy loss within the device. R_S refers to the overall resistance spanning

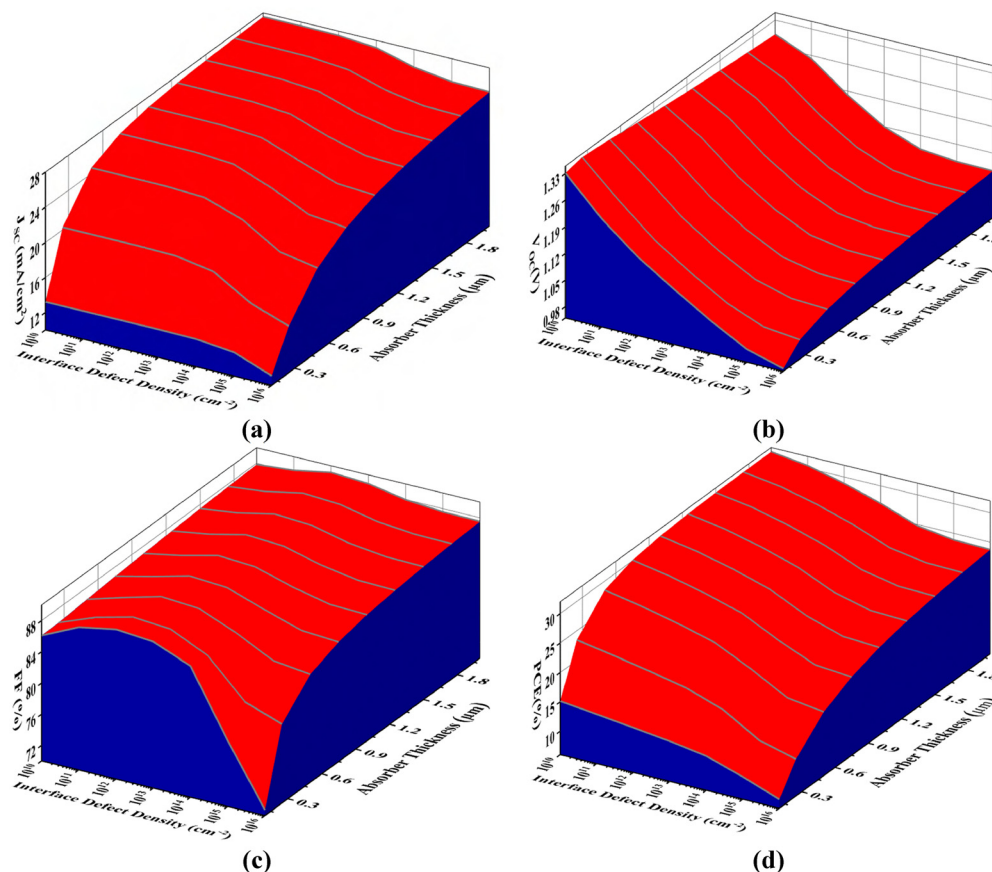**Fig. 6** Simultaneous effect of changing the interface defect density (Sr_3PBr_3/CBTS) on the PV output.

various layers of solar cells. Conversely, R_{SH} arises from the reverse saturation current in PSCs caused by imperfections introduced during fabrication. Here, we investigate the impact of R_S and R_{SH} on solar cell parameters to see the actual behavior. Fig. 8(a) depicts the output parameters, as R_S varies from 1 to 6 Ω cm^2 for the optimized (FTO/SnS$_2$/Sr$_3$PBr$_3$/CBTS/Au) solar cells. It is observed that V_{OC} and J_{SC} remain unchanged across the entire range of R_S values. In the meantime, the FF declines significantly from 81.43% to 64.08%, and the PCE decreases from 30.78% to 26.69%. The notable reduction in FF is ascribed to considerable power loss (P_{loss}) within PSCs under high R_S conditions, which unfavorably impacts their overall performance.[63] As R_S increases, the corresponding rise in power loss (P_{loss}) inside the PSCs directly affects the FF.

Similarly, R_{SH} is varied from 10 to 10^7 Ω cm^2, as shown in Fig. 8(b). In this scenario, J_{SC} exhibits minimal variation across all R_{SH} values. Conversely, the output of all solar cells increases as R_{SH} is increased from 10 to 10^3 Ω cm^2. Beyond this range, a linear relationship is observed.

Fig. 8(c) shows the series resistance dependence of photovoltaic parameters without the HTL. It is observed that V_{OC} is increased with rising series resistance, while other parameters are decreased. Fig. 8(d) displays the variation of photovoltaic parameters with shunt resistance without the HTL and exhibits

a similar trend as in Fig. 8(b) with enhanced values of all the parameters.

3.8. Effect of temperature

The operating temperature of PSCs is vital due to their exposure to ambient atmospheric conditions, necessitating extended durability. Consequently, it is essential to comprehend the degradation mechanisms of solar cells under real world conditions.[64,65] In this context, we systematically varied the working temperature of (FTO/SnS$_2$/Sr$_3$PBr$_3$/CBTS/Au) solar cells from 300 K to 420 K (Fig. 9(a)) to thoroughly evaluate its comprehensive impact. It is evident that as the temperature increases, the values of V_{OC}, FF, and PCE reduce, whereas J_{SC} maintains consistent levels. The decrease in V_{OC} values is due to the heightened vibration of thermally generated electrons at elevated temperatures, making them less stable, and more possibly they recombine with holes, which in turn raises the reverse saturation current (J_O).[66] This trend is evident from the inverse correlation between V_{OC} and J_O, as demonstrated in eqn (6).

$$V_{OC} = \frac{nKT}{q}\left(\ln\left(1 + \frac{J_{SC}}{J_O}\right)\right) \qquad (6)$$
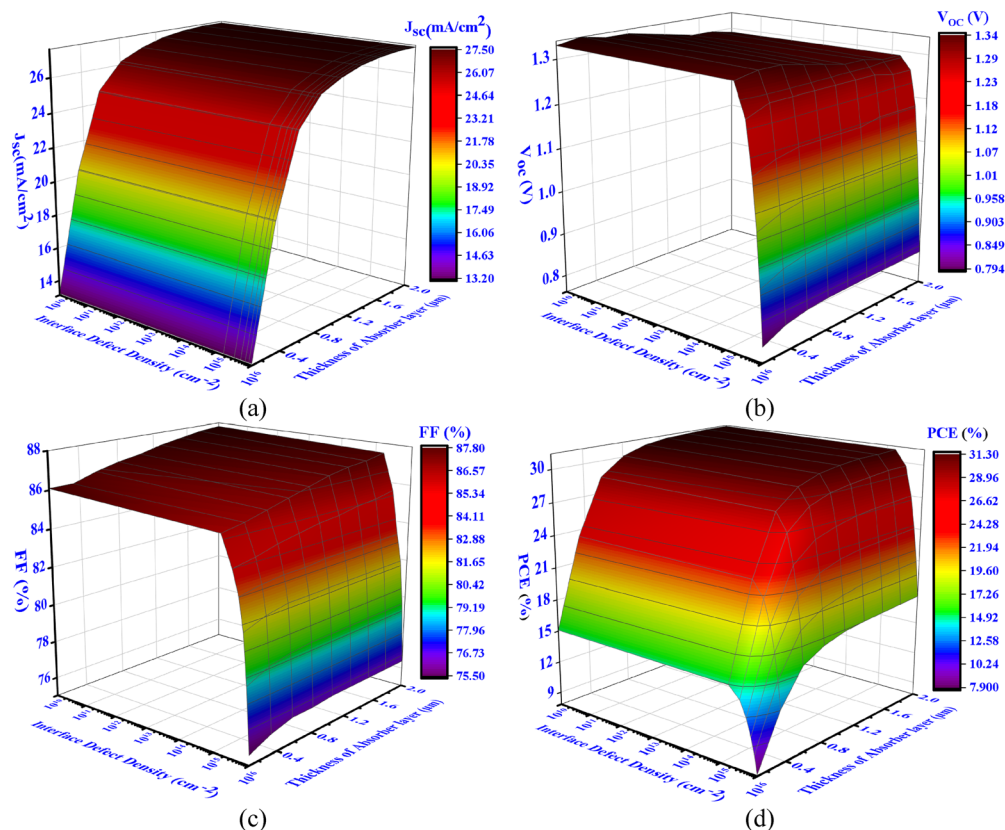
where $\frac{KT}{q}$ represents the thermal voltage.[67]

Fig. 7 The concurrent impact of changing the IDD at the Sr$_3$PBr$_3$/SnS$_2$ interface and the absorber thickness on the performance of the PSC.

Additionally, the physical metrics, including the charge carrier mobility and carrier concentration, are negatively impacted by increasing temperatures, which directly affects the transportation efficiency of charge carriers and consequently reduces the FF of every PSC.[68] This combined reduction in V_{OC} and FF results in a lessening in PCE from 30.78% to 26.39% for CBTS-based solar cells. Fig. 9(b) also illustrates the J–V characteristics at varying temperatures, highlighting the significance of temperature effects. Fig. 9(c) and (d) shows the effect of temperature on PSC's output parameters and the J–V properties of the PSC at different temperatures, without the HTL.

3.9. Current–voltage (J–V) and quantum efficiency (QE) characteristics of the evaluated PSC devices

Fig. 10(a) exhibits the current–voltage (J–V) properties of the device. Furthermore, Table 3 displays the PSC parameters without and with the HTL. The influence of the CBTS HTL in the proposed structure of Sr$_3$PBr$_3$-based solar cells is crystal clear to enhance the photovoltaic performance. Fig. 11(a and b) demonstrates the J–V and QE curves of Sr$_3$PBr$_3$-based solar cells with the HTL (FTO/SnS$_2$/Sr$_3$PBr$_3$/CBTS/Au) and without the HTL (FTO/SnS$_2$/Sr$_3$PBr$_3$/Au). It is evident from Table 3 that the efficiency and FF are improved after incorporating CBTS as the HTL. Under optimized device conditions, the J_{SC} with and without the HTL is found to be 26.839 mA cm^{-2} and 22.970 mA cm^{-2}, respectively. This is attributed to the

interfacial recombination of charge carriers occurring between Sr$_3$PBr$_3$ and the rear contact metal (gold). Fig. 10(b) exhibits a noticeable decline in QE response beyond 820 nm, verifying the band gap of Sr$_3$PBr$_3$, which is found to be 1.528 eV. It is apparent that the QE response of solar cells utilizing CBTS as the HTL is superior to that of PV cells without the HTL. This variance in QE characteristics can be ascribed to the creation of a back surface field after the integration of the HTL.[69,70] Sr$_3$PBr$_3$ serves dual roles as both the absorber and p-type layer in the solar cell structure. Introducing another p-type layer, such as CBTS, improves the overall performance of the PSC. Therefore, CBTS as an HTL is important, aimed at boosting the operational effectiveness of the proposed PSC.

Table 4 compares the simulated photovoltaic performance of the Sr$_3$PBr$_3$-based PSC under ideal and non-ideal conditions. In the ideal case, the device achieves a high PCE of 31.51%, supported by a large V_{OC} (1.377 V), high FF (85.40%), and minimal recombination losses due to negligible series resistance, extremely high shunt resistance, and low bulk defect density (1×10^{10} cm^{-3}). In contrast, the non-ideal case incorporates practical loss mechanisms—namely increased R_S (2 Ω cm^2), reduced R_{SH} (100 Ω cm^2), and a high defect density (1×10^{16} cm^{-3})—which significantly degrade carrier transport and increase recombination. As a result, V_{OC}, J_{SC}, and FF decline sharply, lowering the overall efficiency to 12.15%.
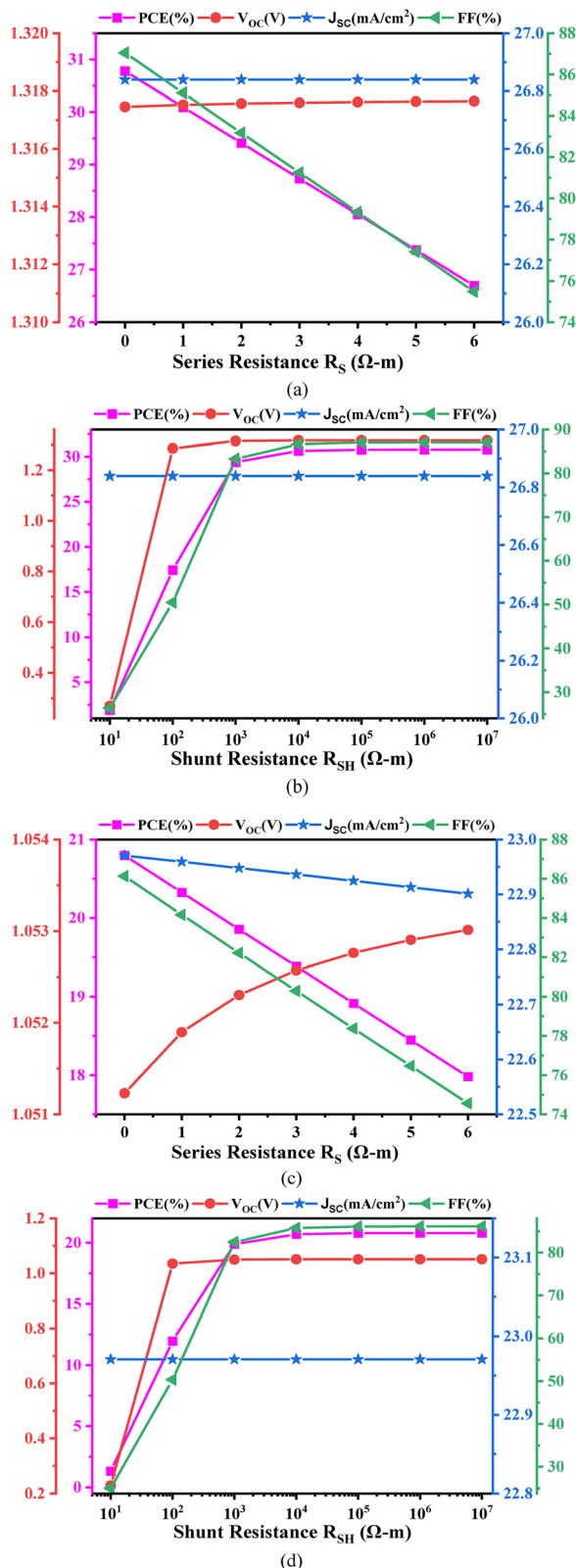
Fig. 8 Influence of (a) series resistance and (b) shunt resistance with the CBTS HTL and (c) series resistance and (b) shunt resistance without the CBTS HTL.

This comparison clearly demonstrates the sensitivity of Sr_3PBr_3 PSCs to resistive and recombination losses and validates that the simulated performance remains consistent with the SQ-limit theoretical framework.

3.10. Machine learning

In our work, the Random Forest algorithm's internal metric was used to generate the feature importance percentages. By calculating each feature's effect on lowering impurity during data splits across the decision tree nodes, this metric evaluates each feature's contribution.[71] The PCE of PSCs was precisely predicted in this study using the Random Forest algorithm, which also identified the key characteristics influencing device performance. With PCE (%) as the desired output, the dataset included ten crucial parameters that are known to affect photovoltaic efficiency. Following data preparation and cleaning, an 80/20 train–test split was used to give the model a large amount of training data while retaining a separate portion for performance evaluation. This study emphasizes important parameters like bandgap, interface defects, and doping concentration as the most important factors influencing solar cell performance, as illustrated in Fig. 11. The analysis provides insightful direction for upcoming photovoltaic technology research and development by highlighting these crucial characteristics. Below are the corresponding relative importance scores for the characteristics that have an impact on the PCE (Table 5):

The findings highlight the significant influence of acceptor density, which is a key factor determining how well photovoltaic devices convert energy. Similarly, the significance of defect levels emphasizes how they improve charge transport inside the device and lower recombination losses. Another important consideration is doping, which has a direct impact on carrier concentration, which is necessary to achieve the best possible device performance as shown in Fig. 5.

The SHAP plot, which is displayed in Fig. 12, shows how different features affect the model's output for forecasting solar cell performance. A data point is represented by each dot, which is colored according to the feature's value, spanning from low (blue) to high (red). For instance, a high defect density (shown by the red dots on the left) significantly reduces the model's output, suggesting a detrimental effect. High acceptor density values, on the other hand, have a positive effect and raise the output. Other characteristics, such as band gap and electron affinity, also exhibit distinct effects, underscoring their importance in the prediction model.

The coefficient of determination (R^2), which shows how much of the variation in the target variables the model can explain, was used to evaluate the predictive performance of the model (see Fig. 13). For PCE, V_{OC}, J_{SC}, and FF, the corresponding R^2 values were 0.9943, 0.9941, 0.9944, and 0.9929, respectively. The model's high effectiveness in elucidating the majority of the variability in these significant output metrics is demonstrated by the high R^2 scores for PCE and V_{OC}. The somewhat reduced R^2 for J_{SC} indicates that although the model successfully reflects the primary patterns,
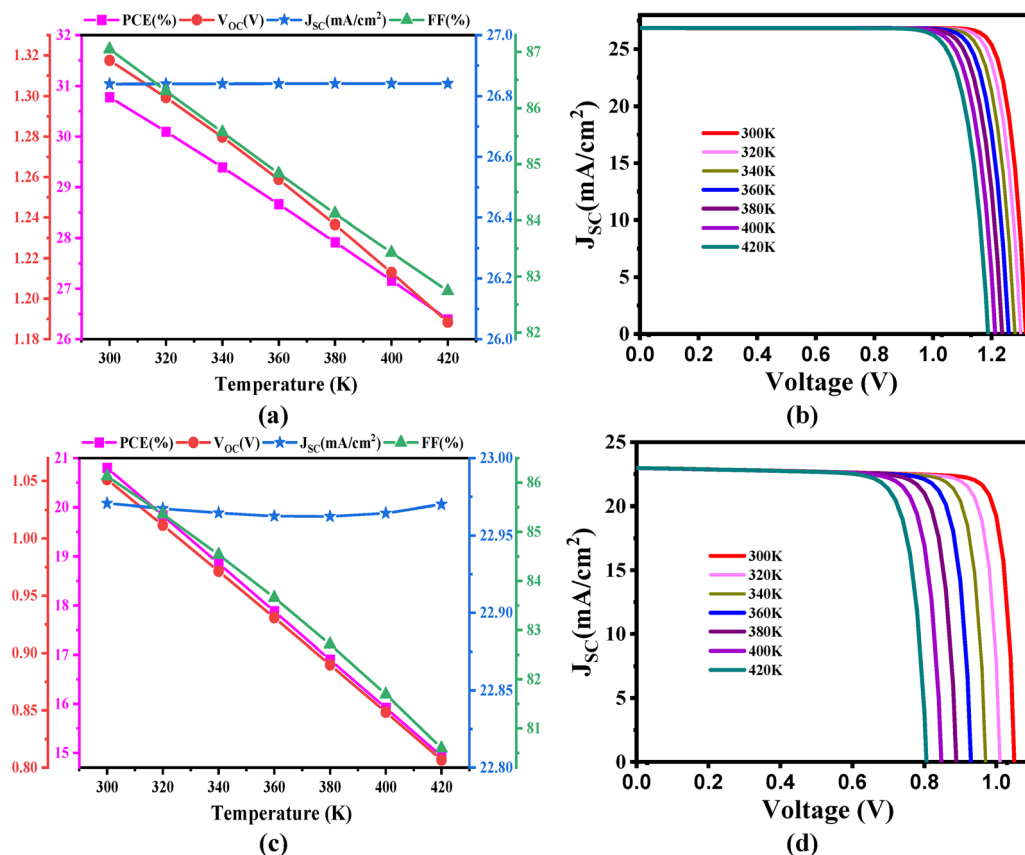
Fig. 9 The effect of temperature on (a) solar cell parameters and (b) the $J-V$ properties with the CBTS HTL and (c) solar cell parameters and (d) the $J-V$ properties without the HTL.
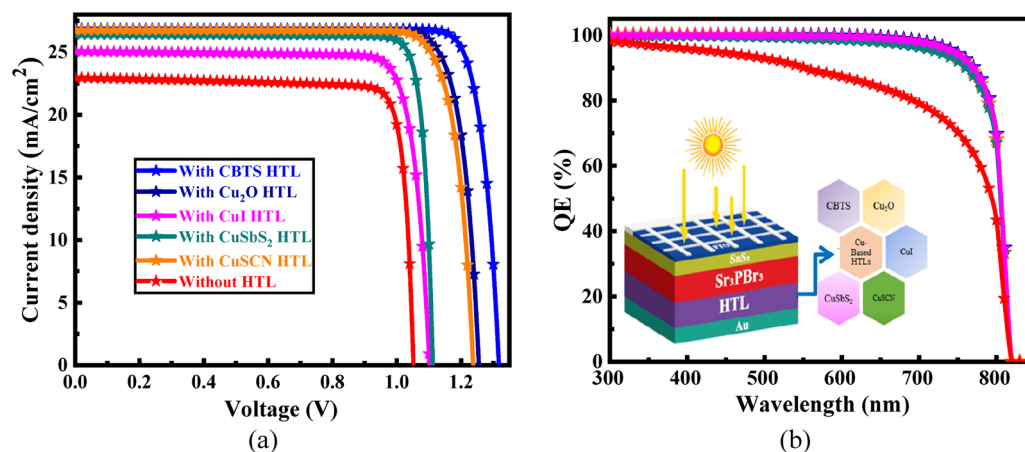

Fig. 10 (a) Current–voltage ($J-V$) characteristics and (b) quantum efficiency (QE) graph of the proposed cell, both with and without the CBTS HTL.

a few variations might still exist, most likely as a result of experimental noise or unaccounted-for variables. The Random Forest algorithm's strong performance in forecasting the behavior of photovoltaic devices is highlighted by its average R^2 of 0.9939.

The reported performance metrics represent theoretical upper limits obtained from SCAPS-1D simulations and

machine learning predictions under idealized conditions. In practical devices, additional non-idealities such as incomplete light absorption, optical reflection, recombination at bulk and interfacial defects, series resistance, and long-term stability issues will inevitably reduce efficiency compared to the simulated values. Thus, the results presented here should be interpreted as benchmarks for guiding experimental optimization
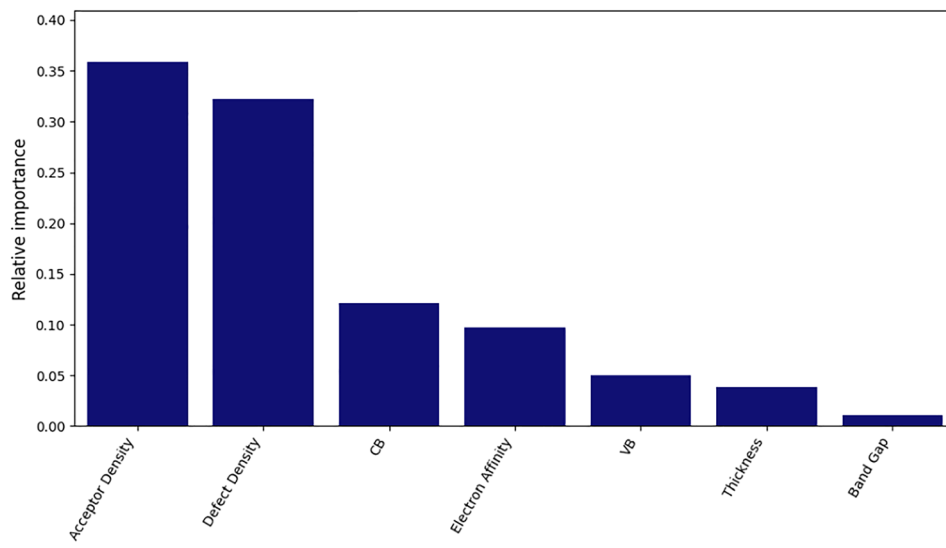
Fig. 11 Several characteristics that are most crucial in the ML mode.

Table 4 The device performance under both ideal and non-ideal parameter conditions

Case	V_{OC} (V)	J_{SC} (mA cm^{-2})	FF (%)	PCE (%)	R_S (Ω cm^2)	R_{SH} (Ω cm^2)	Defect density (cm^{-3})
Ideal	1.377	26.84	85.40	31.51	0	6000	1×10^{10}
Non-ideal	1.0311	23.25	50.62	12.15	2.0	100	1×10^{16}

Table 5 Scores for different important characteristics

Parameters	Value
Acceptor density	0.359222
Defect density	0.322507
CB	0.121174
Electron affinity	0.097420
VB	0.050575
Thickness	0.038474
Band gap	0.010628

Fig. 12 Random forest regression in conjunction with SHAP values was used to examine the impact of unrelated features on the device's PCE.

rather than directly achievable efficiencies, ensuring alignment with realistic photovoltaic expectations.

4. Conclusions

This work presents a comprehensive computational investigation of novel Sr$_3$PBr$_3$-based perovskite solar cells incorporating various inorganic Cu-based hole transport layers (HTLs), modeled using SCAPS-1D. The simulated device structure, FTO/SnS$_2$/Sr$_3$PBr$_3$/CBTS/Au, was systematically optimized by evaluating absorber characteristics under variations in thickness, acceptor density, and defect density, with emphasis on their interdependent effects. Performance enhancement was achieved through fine-tuning donor/acceptor densities, minimizing defect states, and optimizing thicknesses of the ETL, HTL, and absorber layers. The optimal configuration featured an absorber thickness of 1.0 μm, an HTL thickness of 0.05 μm, and a doping concentration of 1.0×10^{17} cm^{-3} for both the absorber and the HTL. Under these conditions, the device achieved an impressive PCE of 30.78%, with J_{SC} = 26.839 mA cm^{-2}, V_{OC} = 1.317 V, and FF = 87.05%. The results confirm that thin SnS$_2$ layers are a promising, non-toxic alternative to conventional CdS as electron transport layers. Additionally, machine learning analysis identified acceptor density and defect density as the most critical determinants of device efficiency, achieving a predictive accuracy of 99.39% when correlating input parameters to photovoltaic performance. These findings highlight the potential of Sr$_3$PBr$_3$ absorbers and Cu-based HTLs for fabricating stable, high-efficiency, lead-free perovskite solar cells, offering a viable route toward environmentally friendly
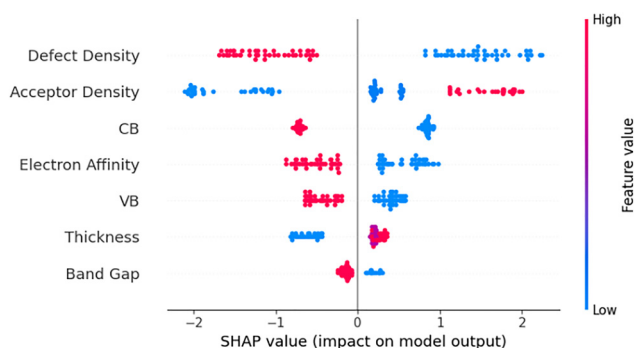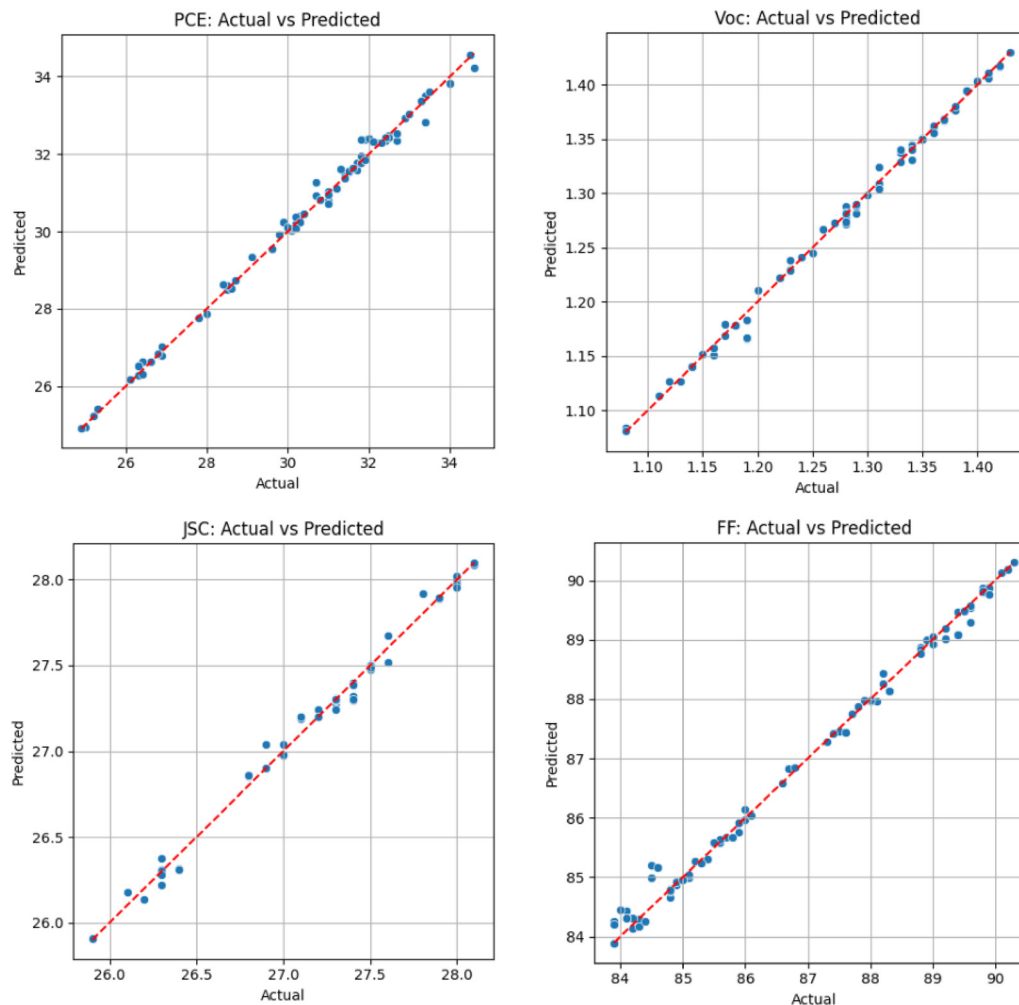
Fig. 13 The assessed and actual values of PCE, V_{OC}, J_{SC}, and FF showing a linear relationship, suggesting that the model predicts these important photovoltaic parameters with little variation.

photovoltaic technologies. It should be noted that this study, based on simulations supported by machine learning, reports theoretical upper limits under idealized conditions; experimental validation is therefore essential, as practical devices will face efficiency reductions from optical, recombination, and stability losses. In addition, stability assessment and large-area scalability remain key directions for future research.

Conflicts of interest

There are no conflicts to declare.

Data availability

All data and code are available *via* this link: https://doi.org/10.5281/zenodo.17244830.

Acknowledgements

References

1 M. S. Reza, M. F. Rahman, A. Kuddus, M. K. A. Mohammed, D. Pal, A. Ghosh, M. R. Islam, S. Bhattarai, I. A. Shaaban and M. Amami, Design and Optimization of High-Performance Novel RbPbBr3-Based Solar Cells with Wide-Band-Gap S-Chalcogenide Electron Transport Layers (ETLs), *ACS Omega*, 2024, **9**, 19824–19836.

2 A. S. Shaikh, S. C. Yadav, A. Srivastava, A. R. Kanwade, M. K. Tiwari, S. M. Rajore, J. A. K. Satrughna, M. Dhonde and P. M. Shirage, Dynamic synergy of tin in the electron-transfer layer and absorber layer for advancing perovskite

solar cells: a comprehensive review, *Energy Adv.*, 2024, **3**, 1505–1552.

3 F. Rehman, I. H. Syed, S. Khanam, S. Ijaz, H. Mehmood, M. Zubair, Y. Massoud and M. Q. Mehmood, Fourth-generation solar cells: a review, *Energy Adv.*, 2023, **2**, 1239–1262.

4 A. Ayyaz, M. Zaman, H. D. Alkhaldi, H. I. Ali, I. Boukhris, S. Bouzgarrou, M. Mana Al-Anazy and Q. Mahmood, Computational screening of appealing perspectives of indium-based halide double perovskites In2AgSbX6 (X = Cl, Br, and I) for energy harvesting technologies, *RSC Adv.*, 2025, **15**, 11128–11145.

5 H. J. Snaith, Present status and future prospects of perovskite photovoltaics, *Nat. Mater.*, 2018, **17**, 372–376.

6 C. Battaglia, A. Cuevas and S. De Wolf, High-efficiency crystalline silicon solar cells: Status and perspectives, *Energy Environ. Sci.*, 2016, **9**, 1552–1576.

7 M. A. Green, E. D. Dunlop, J. Hohl-Ebinger, M. Yoshita, N. Kopidakis and X. Hao, Solar cell efficiency tables (Version 58), *Prog. Photovoltaics Res. Appl.*, 2021, **29**, 657–667.

8 K. Yamamoto, K. Yoshikawa, H. Uzu and D. Adachi, High-efficiency heterojunction crystalline Si solar cells, *Jpn. J. Appl. Phys.*, 2018, **57**, 08RB20.

9 C. Qiu, R. Cao, C.-X. Zhang, C. Zhang, D. Guo, T. Shen, Z.-Y. Liu, Y.-Y. Hu, F. Wang and H.-X. Deng, First-Principles Study of Intrinsic Point Defects of Monolayer GeS, *Chin. Phys. Lett.*, 2021, **38**, 26103.

10 A. Aissat, L. Chenini, A. Laidouci, S. Nacer and J. P. Vilcot, Improvement in the efficiency of solar cells based on the ZnSnN2/Si structure, *Mater. Sci. Eng. B*, 2024, **300**, 117071.

11 B. Sultana, F. Rahman, A. Chandra, M. Mia, A. Ijajul, A. Irfan, A. Rasool and D. Haque, Materials Science & Engineering B A novel design and optimization of Si based high performance double absorber heterojunction solar cell, *Mater. Sci. Eng. B*, 2024, **304**, 117360.

12 A. A. Yaroshevsky, Abundances of chemical elements in the Earth's crust, *Geochem. Int.*, 2006, **44**, 48–55.

13 D. Luo, W. Jang, D. Babu, M. Kim, D. H. Wang and A. Kyaw, Recent Progress in Organic Solar Cells Based on Non-Fullerene Acceptors: Materials to Devices, *J. Mater. Chem. A*, 2022, 3255–3295.

14 S. F. Hoefler, G. Trimmel and T. Rath, Progress on lead-free metal halide perovskites for photovoltaic applications: a review, *Monatsh. Chem.*, 2017, **148**, 795–826.

15 G. Niu, X. Guo and L. Wang, Review of recent progress in chemical stability of perovskite solar cells, *J. Mater. Chem. A*, 2015, **3**, 8970–8980.

16 B. Conings, J. Drijkoningen, N. Gauquelin, A. Babayigit, J. D'Haen, L. D'Olieslaeger, A. Ethirajan, J. Verbeeck, J. Manca, E. Mosconi, F. De Angelis and H.-G. Boyen, Intrinsic Thermal Instability of Methylammonium Lead Trihalide Perovskite, *Adv. Energy Mater.*, 2015, **5**, 1500477.

17 M. Shirayama, H. Kadowaki, T. Miyadera, T. Sugita, M. Tamakoshi, M. Kato, T. Fujiseki, D. Murata, S. Hara, T. N. Murakami, S. Fujimoto, M. Chikamatsu and H. Fujiwara, Optical Transitions in Hybrid Perovskite Solar Cells: Ellipsometry, Density Functional Theory, and Quantum Efficiency Analyses for CH$_3$NH$_3$PbI$_3$, *Phys. Rev. Appl.*, 2016, **5**, 14012.

18 F. Khan, F. Rasheed J, T. Alshahrani, S. Kashif Ali, A. M. Alanazi, A. H. Alsehli, M. M. Alsowayigh and N. Elamin Ahmed, Investigations on performance parameters of graphene interfacial layer modified FASnI3: Zn-based lead-free perovskite solar cells, *Mater. Sci. Eng. B*, 2024, **301**, 117209.

19 Q. Fan, G. V. Biesold-McGee, J. Ma, Q. Xu, S. Pan, J. Peng and Z. Lin, Lead-Free Halide Perovskite Nanocrystals: Crystal Structures, Synthesis, Stabilities, and Optical Properties, *Angew. Chem. Int. Ed. Engl.*, 2020, **59**, 1030–1046.

20 Z. Xiao, Z. Song and Y. Yan, From Lead Halide Perovskites to Lead-Free Metal Halide Perovskites and Perovskite Derivatives, *Adv. Mater.*, 2019, **31**, 1803792.

21 M. K. Hossain, S. Bhattarai, A. A. Arnab, M. K. A. Mohammed, R. Pandey, M. H. Ali, M. F. Rahman, M. R. Islam, D. P. Samajdar, J. Madan, H. Bencherif, D. K. Dwivedi and M. Amami, Harnessing the potential of CsPbBr3-based perovskite solar cells using efficient charge transport materials and global optimization, *RSC Adv.*, 2023, **13**, 21044–21062.

22 B. Ghosh, B. Wu, H. K. Mulmudi, C. Guet, K. Weber, T. C. Sum, S. Mhaisalkar and N. Mathews, Limitations of Cs(3)Bi(2)I(9) as Lead-Free Photovoltaic Absorber Materials, *ACS Appl. Mater. Interfaces*, 2018, **10**, 35000–35007.

23 A. Husainat, W. Ali, P. Cofie, J. Attia and J. Fuller, Simulation and Analysis of Methylammonium Lead Iodide (CH3NH3PbI3) Perovskite Solar Cell with Au Contact Using SCAPS 1D Simulator, *Am. J. Opt. Photonics*, 2019, **7**, 33–40.

24 A. Tara, V. Bharti, S. Sharma and R. Gupta, Device simulation of FASnI3 based perovskite solar cell with Zn(O0.3, S0.7) as electron transport layer using SCAPS-1D, *Opt. Mater.*, 2021, **119**, 111362.

25 W. Yan, Y. Liu, Y. Zang, J. Cheng, Y. Wang, L. Chu, X. Tan, L. Liu, P. Zhou and Z. Zhong, Machine learning enabled development of unexplored perovskite solar cells with high efficiency, *Nano Energy*, 2022, **99**, 107394.

26 D. O. Obada, S. B. Akinpelu, S. A. Abolade, E. Okafor, A. M. Ukpong, S. R. Kumar and A. Akande, Lead-Free Double Perovskites: A Review of the Structural, Optoelectronic, Mechanical, and Thermoelectric Properties Derived from First-Principles Calculations, and Materials Design Applicable for Pedagogical Purposes, *Crystals*, 2024, **14**, 1–26.

27 B. Martín-García, D. Spirito, M.-L. Lin, Y. Leng, S. Artyukhin, P.-H. Tan and R. Krahne, Adv. Opt. Mater. - Back cover - Low-Frequency Phonon Modes in Layered Silver-Bismuth Double Perovskites: Symmetry, Polarity, and Relation to Phase Transitions, 2022, **10**.

28 Z. Zhang, Y. Liang, H. Huang, X. Liu, Q. Li, L. Chen and D. Xu, Stable and Highly Efficient Photocatalysis with Lead-Free Double-Perovskite of Cs(2) AgBiBr(6), *Angew. Chem., Int. Ed.*, 2019, **58**, 7263–7267.

29 L. Yin, H. Wu, W. Pan, B. Yang, P. Li, J. Luo, G. Niu and J. Tang, Controlled Cooling for Synthesis of Cs2AgBiBr6

Single Crystals and Its Application for X-Ray Detection, *Adv. Opt. Mater.*, 2019, **7**, 1900491.

30 C. Liu, Y. Yang, O. A. Syzgantseva, Y. Ding, M. A. Syzgantseva, X. Zhang, A. M. Asiri, S. Dai and M. K. Nazeeruddin, α-CsPbI3 Bilayers via One-Step Deposition for Efficient and Stable All-Inorganic Perovskite Solar Cells, *Adv. Mater.*, 2020, **32**, 2002632.

31 Z. Jin, Z. Zhang, J. Xiu, H. Song, T. Gatti and Z. He, A critical review on bismuth and antimony halide based perovskites and their derivatives for photovoltaic applications: recent advances and challenges, *J. Mater. Chem. A*, 2020, **8**, 16166–16188.

32 S. Islam, J. I. Chy, D. D. Ria, A. Bakkar, A. R. Chaudhry, Md. F. Hossain, A. Irfan and Md. F. Rahman, Next-generation dual absorber solar cell design with Ca3AsI3 and Sr3PBr3 perovskites and MoO3, *Energy Adv.*, 2025, 1383–1400.

33 S. Joifullah, M. A. Hossain, M. Al Yeamin, M. M. Haque, R. K. Pingak, N. F. A. Mohammad, M. S. Abu-Jafar, A. A. Mousa and A. Hosen, First-principles investigation of pressure-modulated structural, electronic, mechanical, and optical characteristics of Sr3PX3 (X = Cl, Br) for enhanced optoelectronic application, *Opt. Quantum Electron.*, 2024, 1463.

34 M. F. Rahman, M. Harun-Or-Rashid, M. R. Islam, A. Irfan, A. R. Chaudhry, M. A. Rahman and S. Al-Qaisi, A Deep Analysis and Enhancing Photovoltaic Performance Above 31% with New Inorganic RbPbI$_3$-Based Perovskite Solar Cells via DFT and SCAPS-1D, *Adv. Theory Simul.*, 2024, 2400476.

35 Y. Wei, Z. Ma, X. Zhao, J. Yin, Y. Wu, L. Zhang and M. Zhao, Improving the performance of Cu2ZnSn(S,Se)4 thin film solar cells by SCAPS simulation, *Mater. Sci. Eng. B*, 2024, **303**, 117296.

36 A. Ait Abdelkadir and M. Sahal, Theoretical development of the CZTS thin-film solar cell by SCAPS-1D software based on experimental work, *Mater. Sci. Eng. B*, 2023, **296**, 116710.

37 A. Hosen, M. S. Mian and S. R. Al Ahmed, Improving the Performance of Lead-Free FASnI$_3$-Based Perovskite Solar Cell with Nb$_2$O$_5$ as an Electron Transport Layer, *Adv. Theory Simul.*, 2023, **6**, 2200652.

38 A. Hosen, M. S. Mian and S. R. Al Ahmed, Improving the Performance of Lead-Free FASnI3-Based Perovskite Solar Cell with Nb2O5 as an Electron Transport Layer, *Adv. Theory Simul.*, 2023, **2200652**, 1–13.

39 A. Morales-acevedo, Fundamentals of solar cell physics revisited: Common pitfalls when reporting calculated and measured photocurrent density, open-circuit voltage, and efficiency of solar cells, *Sol. Energy*, 2023, **262**, 111774.

40 N. Obare, W. Isoe, A. Nalianya, M. Mageto and V. Odari, Numerical study of copper antimony sulphide (CuSbS(2)) solar cell by SCAPS-1D, *Heliyon*, 2024, **10**, e26896.

41 V. Deswal, S. Kaushik, R. Kundara and S. Baghel, Numerical simulation of highly efficient Cs2AgInBr6-based double perovskite solar cell using SCAPS 1-D, *Mater. Sci. Eng. B*, 2024, **299**, 117041.

42 A. Owolabi, H. Ali, M. Ismaila Salami, U. Ushiekpan, J. Bamikole and M. Madugu, Optimization of Lead Base Perovskite Solar Cell with ZnO and CuI as Electron Transport Material and Hole Transport Material Using SCAPS-1D, *Malays. J. Appl. Sci.*, 2021, **6**, 69–84.

43 K. Deepak, G. S. C. Reddy and C. Tiwari, Performance Analysis of SnO2/CsSnGeI3/CuSCN perovskite solar cells using SCAPS 1D Simulator, *J. Phys.: Conf. Ser.*, 2023, **2571**, 12023.

44 D. A. Fentahun, A. Tyagi and K. K. Kar, Numerically investigating the AZO/Cu2O heterojunction solar cell using ZnO/CdS buffer layer, *Optik*, 2021, **228**, 166228.

45 M. Salah, A. Zekry, A. Shaker, M. Abouelatta-Ebrahim, M. Moussa and A. Saeed, Investigation of Electron Transport Material-Free Perovskite/CIGS Tandem Solar Cell, *Energies*, 2022, **15**, 6326.

46 S. Tripathi, B. Kumar and D. K. Dwivedi, Numerical simulation of non-toxic In2S3/SnS2 buffer layer to enhance CZTS solar cells efficiency by optimizing device parameters, *Optik*, 2021, **227**, 166087.

47 A. Ghosh, F. Ahmed, M. Ferdous, M. M. J. Juhi, M. F. I. Buian, A. A. Miazee, M. Sajid, M. Maniruzzaman, A. Tighezza, M. Ahmmed and M. Islam, Strain-Induced Changes in the Electronic, Optical and Mechanical Properties of the Inorganic Cubic Halide Perovskite Sr3PBr3 with FP-DFT, *J. Phys. Chem. Solids*, 2024, 112053.

48 M. A. Ashraf and I. Alam, Numerical simulation of CIGS, CISSe and CZTS-based solar cells with In2S3 as buffer layer and Au as back contact using SCAPS 1D, *Eng. Res. Express*, 2020, **2**, 35015.

49 L. I. Nykyruy, R. S. Yavorskyi, Z. R. Zapukhlyak, G. Wisz and P. Potera, Evaluation of CdS/CdTe thin film solar cells: SCAPS thickness simulation and analysis of optical properties, *Opt. Mater.*, 2019, **92**, 319–329.

50 N. K. Bansal, S. Mishra, H. Dixit, S. Porwal, P. Singh and T. Singh, Machine Learning in Perovskite Solar Cells: Recent Developments and Future Perspectives, *Energy Technol.*, 2023, **11**, 2300735.

51 K. T. Arockiya-Dass, K. Sekar and L. Marasamy, Theoretical Insights of Degenerate ZrS2 as a New Buffer for Highly Efficient Emerging Thin-Film Solar Cells, *Energy Technol.*, 2023, **11**, 2300333.

52 G. Kumar, B. K. Ravidas, S. Bhattarai, M. K. Roy and D. P. Samajdar, Exploration of the photovoltaic properties of oxide-based double perovskite Bi2FeCrO6 using an amalgamation of DFT with spin–orbit coupling effect and SCAPS-1D simulation approaches, *New J. Chem.*, 2023, **47**, 18640–18658.

53 M. F. Rahman, A. Lubaba, L. Ben Farhat, S. Ezzine, M. H. Rahman and M. Harun-Or-Rashid, Efficiency enhancement above 31% of Sb2Se3 solar cells with optimizing various BSF layer, *Mater. Sci. Eng. B*, 2024, **307**, 117527.

54 M. Ferdous Rahman, M. Al Ijajul Islam, M. Chowdhury, L. Ben Farhat, S. Ezzine and A. T. M. Saiful Islam, Efficiency improvement of CsSnI3 based heterojunction solar cells with P3HT HTL: A numerical simulation approach, *Mater. Sci. Eng. B*, 2024, **307**, 117524.

55 M. Ferdous Rahman, M. Naim Hasan Toki, A. Kuddus, M. K. A. Mohammed, M. Rasidul Islam, S. Bhattarai, J. Madan, R. Pandey, R. Marzouki and M. Jemmali, Boosting

efficiency above 30% of novel inorganic Ba3SbI3 perovskite solar cells with potential ZnS electron transport layer (ETL), *Mater. Sci. Eng. B*, 2024, **300**, 117073.

56 M. K. Hossain, G. F. Toki, A. Kuddus, M. Rubel, M. M. Hossain, H. Bencherif, M. Rahman, M. R. Islam and M. Mushtaq, An extensive study on multiple ETL and HTL layers to design and simulation of high-performance lead-free CsSnCl3-based perovskite solar cells, *Sci. Rep.*, 2023, **23**, 2521.

57 A. Raj, M. Kumar, H. Bherwani, A. Gupta and A. Anshul, Evidence of improved power conversion efficiency in lead-free CsGeI 3 based perovskite solar cell heterostructure via scaps simulation, *J. Vac. Sci. Technol., B*, 2021, **39**, 12401.

58 H. K. Ibrahim, A. M. A. Sabaawi and Q. T. Algwari, Study of defects in CH3NH3PbI3-based perovskite solar cells, *IOP Conf. Ser.: Mater. Sci. Eng.*, 2021, **1152**, 12032.

59 A. W. Welch, L. L. Baranowski, H. Peng, H. Hempel, R. Eichberger, T. Unold, S. Lany, C. Wolden and A. Zakutayev, Trade-Offs in Thin Film Solar Cells with Layered Chalcostibite Photovoltaic Absorbers, *Adv. Energy Mater.*, 2017, **7**, 1601935.

60 S. Mushtaq, S. Tahir, A. Ashfaq, R. Sebastian Bonilla, M. Haneef, R. Saeed, W. Ahmad and N. Amin, Performance optimization of lead-free MASnBr3 based perovskite solar cells by SCAPS-1D device simulation, *Sol. Energy*, 2023, **249**, 401–413.

61 K. Shivesh, I. Alam, A. K. Kushwaha, M. Kumar and S. V. Singh, Investigating the theoretical performance of Cs2TiBr6-based perovskite solar cell with La-doped BaSnO3 and CuSbS2 as the charge transport layers, *Int. J. Energy Res.*, 2022, **46**, 6045–6064.

62 J. Cerdà, J. Arbiol, R. Diaz, G. Dezanneau and J. R. Morante, Synthesis of perovskite-type BaSnO3 particles obtained by a new simple wet chemical route based on a sol–gel process, *Mater. Lett.*, 2002, **56**, 131–136.

63 G. Baysset and G. Baysset, Modélisation et simulation thermique de différentes architectures de chaine de traction d' un véhicule hybride To cite this version: HAL Id: tel-04041404.

64 P. Singh and N. M. Ravindra, Temperature dependence of solar cell performance—an analysis, *Sol. Energy Mater. Sol. Cells*, 2012, **101**, 36–45.

65 A. Raj, M. Kumar, A. Kumar, A. Laref and A. Anshul, Investigating the potential of lead-free double perovskite Cs2AgBiBr6 material for solar cell applications: A theoretical study, *Int. J. Energy Res.*, 2022, **46**, 13801–13819.

66 K. Djessas, I. Bouchama, K. Medjnoun and A. Bouloufa, Simulation and performance analysis of superstrate Cu(In,Ga)Se2 solar cells using nanostructured $Zn_{1-x}V_xO$ thin films, *Int. J. Nanotechnol.*, 2014, 854–860.

67 M. K. Hossain, G. F. Toki, I. Alam, R. Pandey, D. Samajdar, M. Rahman, M. R. Islam, M. Rubel, H. Bencherif, J. Madan and M. Mohammed, Numerical simulation and optimization of CsPbI3-based perovskite solar cell to enhance the power conversion efficiency, *New J. Chem.*, 2023, **47**, 4801–4817.

68 K. Chakraborty, M. G. Choudhury and S. Paul, Numerical study of Cs2TiX6 (X = Br−, I−, F− and Cl−) based perovskite solar cell using SCAPS-1D device simulation, *Sol. Energy*, 2019, **194**, 886–892.

69 A. Sunny and S. R. Al Ahmed, Numerical Simulation and Performance Evaluation of Highly Efficient Sb2Se3 Solar Cell with Tin Sulfide as Hole Transport Layer, *Phys. Status Solidi*, 2021, **258**, 2000630.

70 A. Maiti, S. Chatterjee and A. Pal, Sulfur-Vacancy Passivation in Solution-Processed Sb 2 S 3 Thin-Films: Influence on Photovoltaic-Interfaces, *ACS Appl. Energy Mater.*, 2020, 810–821.

71 M. Hasanzadeh Azar, S. Aynehband, H. Abdollahi, H. Alimohammadi, N. Rajabi, S. Angizi, V. Kamraninejad, R. Teimouri and A. Simchi, SCAPS Empowered Machine Learning Modelling of Perovskite Solar Cells: Predictive Design of Active Layer and Hole Transport Materials, *Photonics*, 2023, **10**, 271.